International Symposium
On Turbulence and Shear Flow
Phenomena (TSFP-9)
June 30 - July 3, 2015 *Melbourne, Australia*

A COMPARISON OF THE DECAY OF ENERGY IN THE WAKE OF FRACTAL AND CLASSICAL GRIDS

R. Jason Hearst & Philippe Lavoie
Institute for Aerospace Studies
University of Toronto
Toronto, Ontario, Canada, M3H 5T6
lavoie@utias.utoronto.ca

ABSTRACT

A square-fractal-element grid and two regular grids, all with the same blockage, are used to investigate how the produced turbulence differs. The square-fractal-element grid is made-up of a 12×8 array of small square fractals mounted to a background mesh. For a constant inlet Reynolds number, Re_M, it is found that the turbulent kinetic energy power-law decay exponent is comparable for all three grids in the far-field, although the fractal-based grid produces an extended non-equilibrium region relative to the other two grids. The normalized dissipation, C_ε, is found to be approximately described by Re_M/Re_L in the non-equilibrium region, becoming approximately constant in the far-field. A correlation is also found between C_ε and normalized Reynolds stress, $\langle uv \rangle / u'v'$, across both the non-equilibrium region and the far-field. Finally, non-equilibrium and far-field spectra are compared at fixed Re_λ across all three grids. It is found that the far-field spectra are reasonably collapsed for all three grids for a given Re_λ. However, if a non-equilibrium spectrum at a location where $\langle uv \rangle \neq 0$ is compared at a given Re_λ to a far-field spectrum where $\langle uv \rangle \approx 0$, then the non-equilibrium spectrum is nearer to $k^{-5/3}$. This result appears to be closely related to the existence of $\langle uv \rangle$ that is able to penetrate to scales associated with the scaling range.

INTRODUCTION

Interest in fractal and multi-scale generated flows has been piqued in recent years. In the first wind tunnel experiments with fractal-based grids, Hurst & Vassilicos (2007) found rapid decay of the turbulent kinetic energy over an extended region in the wake of a space-filling square fractal grid, which contrasted with traditional expectations. Specifically, Valente & Vassilicos (2011) found a decay exponent of $n \approx -2.5$ for the power-law decay of the turbulent kinetic energy, typically of the form

$$\left\langle q^2 \right\rangle \sim (x - x_0)^n \tag{1}$$

where $\left\langle q^2 \right\rangle = \left\langle u^2 \right\rangle + \left\langle v^2 \right\rangle + \left\langle w^2 \right\rangle$ is twice the turbulent kinetic energy, x is downstream distance, and x_0 is a virtual origin. This contrasts with theoretical expectations and previous regular grid turbulence measurements where $-1 \geq n \geq -1.4$. It has also been shown that the normalized dissipation rate of turbulent kinetic energy,

$$C_\varepsilon = \frac{\langle \varepsilon \rangle L}{\left\langle u^2 \right\rangle^{3/2}} \tag{2}$$

grew rapidly downstream of a fractal. Remarkably, this rapid evolution has been shown to approximately follow

$$C_\varepsilon \sim \frac{Re_M}{Re_L} \tag{3}$$

at several different positions in several different flows (Valente & Vassilicos, 2012, 2014; Goto & Vassilicos, 2015). In (3), $Re_M = U_0 M/\nu$ is the global inlet Reynolds number where U_0 is the velocity immediately upstream of the grid, and M is the grid mesh length, and $Re_L = u'L/\nu$ is a local Reynolds number based on the integral scale, L. Rapid growth of C_ε also contrasts with theoretical expectations that C_ε should be constant for sufficiently high Reynolds numbers. Finally, it has been suggested that the turbulence produced by fractal grids is able to produce a long (two decade) scaling range with a shape near $k^{-5/3}$ for lower Re_λ than regular grids (Mazellier & Vassilicos, 2010; Valente & Vassilicos, 2011). These three properties of the turbulence produced in the wake of fractals, and possibly all grids (Valente & Vassilicos, 2012; Krogstad & Davidson, 2012; Isaza *et al.*, 2014), are representative of what has been coined 'non-equilibrium' turbulence.

Using a square-fractal-element grid, composed of 12×8 mesh of small square fractals, Hearst & Lavoie (2014*a*) showed that if measurements are performed downstream of $x/M \approx 20$ (where $M = L_0$ is the length of the largest element in the grid), then a region where $n \approx -1.37$ and $C_\varepsilon \sim$ constant does exist in the wake of their fractal-based grid; earlier measurements had been performed in the region $x/M < 19$. Later, Nagata *et al.* (2013), Valente & Vassilicos (2014) and Hearst & Lavoie (2014*b*) all demonstrated that the near-field ($x/M < 20$) of fractal wakes experience non-zero, non-uniform transverse transport of turbulent kinetic energy and turbulent production. The latter authors suggested that these properties were responsible for the anomalous behaviour in the wake of fractals that, in their experiments, only occurred in the region where these factors were present.

The present study employs two regular grids with similar physical parameters to a square-fractal-element grid

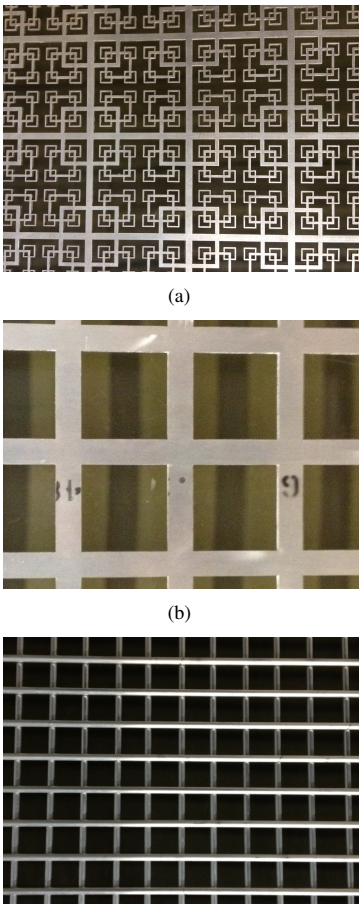

(a)

(b)

(c)

Figure 1. Photographs of a nominally 340 mm × 260 mm area of each of the 1200 mm × 800 mm grids; (a) $Fs39$, (b) $Sq39$, (c) $Rd38$ (Hearst & Lavoie, 2014*a*).

to assess the differences and similarities between regular grids and fractal grids in light of the new research in the field. Although similar studies have been conducted in the past, the focus here is on matching either the global inlet Reynolds number, $Re_M = U_0 M/\nu$, or the local Reynolds number based on the Taylor microscale, $Re_\lambda = \langle u^2 \rangle^{1/2} \lambda/\nu$ (where λ is the Taylor microscale). In particular, we investigate the power-law decay exponents and C_ε for matched Re_M, and spectra produced in different regions of the various grid wakes but at the same Re_λ.

EXPERIMENTAL PROCEDURE

Measurements of the turbulence produced by three different passive grids were conducted in the low-speed recirculating wind tunnel at the University of Toronto Institute for Aerospace Studies. The test-section is 1.2 m × 0.8 m in cross-section and 5 m long, with a background turbulence intensity of approximately 0.06%. Hot-wire anemometry was used to measure the velocity fluctuations. In particular, a single-wire, X-wire, and nano-scale thermal anemometry probe (NSTAP) were used simultaneously, and were operated by a Dantec StreamLine constant temperature anemometer. Unless stated otherwise, measurements of the streamwise velocity presented here are from the NSTAP; for more information on NSTAPs, see Vallikivi *et al.* (2011).

The wind tunnel was fit with a 1.23:1 secondary contraction with the contracted region beginning 0.57 m downstream of the grids. Secondary contractions have been effectively used in the past to improve the level of global isotropy in the flow (Comte-Bellot & Corrsin, 1966). We employ one here to marginalize the effects of anisotropy. A consequence of the secondary contraction is that the longitudinal position is measured relative to the transit time of turbulent advection from the grid, given by $t = \int_0^x (1/U(s))\,\mathrm{d}s$, and hence downstream position is given as $U_0 t/M$, rather than the typical x/M.

The three grids tested are shown in Figure 1 and consist of two regular grids ($Sq39$ and $Rd38$) and a square-fractal-element grid ($Fs39$). $Fs39$ is the same square-fractal-element grid as used by Hearst & Lavoie (2014*a*,*b*) and consists of several small square fractal elements mounted to a 12×8 background mesh with $L_0 = M = 100$ mm. $Sq39$ was designed to match the mesh length, M, and blockage, σ, of $Fs39$, and $Rd38$ was designed to approximately match the thickness of the thickest element, τ_0, and σ to $Fs39$. Details of the various grids are given in Table 1.

The hot-wires were traversed using an automated system in both the transverse and longitudinal directions. Transverse scans were performed at $x = 1.25$ m, 2.00 m, 3.25 m, and 4.50 m, in the range $-0.25\text{ m} \le y \le +0.20$ m, to investigate the homogeneity of the flow. Longitudinal measurements were performed along the $(y,z) = (+15,0)$ mm axis where U was closest to a constant along the tunnel length for all three grids. Longitudinal scans were performed in the region $0.75\text{ m} \le x \le 4.90$ m. Each longitudinal scan consisted of measurements at 95 or more x-positions. A range of inlet Reynolds numbers, Re_M, were used to produce a variety of Re_λ. The decay of energy is compared between grids for a matched $Re_M = 28{,}500$.

HOMOGENEITY AND ISOTROPY

Transverse measurements in the wake of $Rd38$ and $Sq39$ reveal that the produced turbulence is approximately homogeneous in U to within $\pm 1\%$ from $x = 1.25$ m ($U_0 t/M = 34.2$ for $Rd38$, and $U_0 t/M = 10.9$ for $Sq39$). Downstream of $Fs39$, however, the flow did not homogenize until approximately $x = 2.00$ m ($U_0 t/M = 17.0$). As such, the regular grid with the same M and σ as $Fs39$ homogenizes more rapidly in both normalized space and dimensional space.

The transverse scans also revealed that there was non-zero, non-uniform production and transverse transport of turbulent kinetic energy in the wake of $Fs39$. The production is shown for the wakes of all three grids in Figure 2, where it is also shown that for the regular grids the production is negligible from the first transverse measurement position. The production in the wake of $Fs39$ rapidly diminished with $U_0 t/M$, and by $U_0 t/M = 17.0$ was negligible. Other studies have also measured diminishing production with streamwise distance (Nagata *et al.*, 2013; Valente & Vassilicos, 2014; Hearst & Lavoie, 2014*b*).

The secondary contraction collapses the global isotropy ratio for all three grids to $u'/v' = 1.10 \pm 0.05$ for $U_0 t/M > 15$, identifying that any far-field differences we observe are not related to difference in global isotropy. The local isotropy, $\langle (\partial v/\partial x)^2 \rangle / \langle (\partial u/\partial x)^2 \rangle$, takes on values of 2.1 for $Rd38$ and $Fs39$, and 1.8 for $Sq39$, all of which are

Table 1. Grid dimensions and properties; lengths and thicknesses are given in mm. For $Fs39$, L_i, and τ_i, with $i = 0, 1, 2, 3$, represent the length and the thickness, respectively, of the elements in the square-fractal-element grid from largest to smallest.

Grid	$L_0 = M$	L_1	L_2	L_3	τ_0	τ_1	τ_2	τ_3	σ	Type
$Fs39$	100.0	55.6	24.7	11.0	6.7	4.1	2.5	1.5	0.39	fractal-element
$Sq39$	100.0	–	–	–	22.0	–	–	–	0.39	planar regular
$Rd38$	32.0	–	–	–	6.8	–	–	–	0.38	bi-planar round-rod

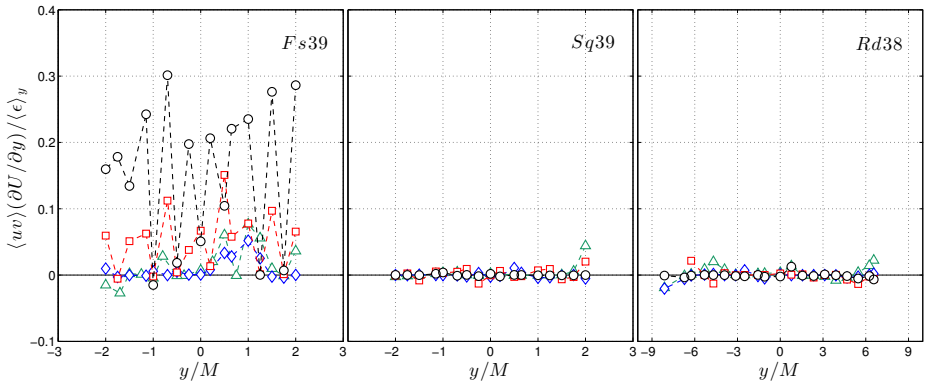

Figure 2. Transverse profiles of the production of turbulent kinetic energy for each grid; (○) $x = 1.25$ m, (□) $x = 2.00$ m, (◇) $x = 3.25$ m, (△) $x = 4.50$ m.

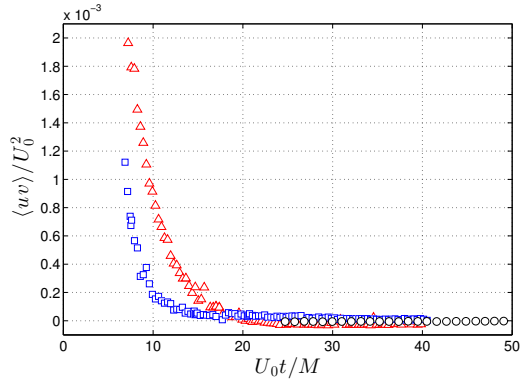

Figure 3. Evolution of the Reynolds stress at $Re_M = 28,500$. (△) $Fs39$, (□) $Sq39$, (○) $Rd38$.

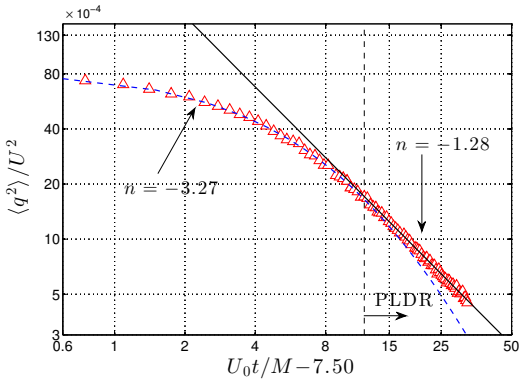

Figure 4. Decay of turbulent kinetic energy with power-law fits for $Fs39$ at $Re_M = 28,500$.

within 10% of the isotropic expectation that this ratio should take on a value of 2.

In Figure 3 the streamwise evolution of the normalized Reynolds stress, $\langle uv \rangle / U_0^2$, is shown. The wakes of both $Fs39$ and $Sq39$ experience non-zero $\langle uv \rangle$ close to the grid which diminishes with streamwise position. The Reynolds stress in the wake of $Rd38$ is always near zero, as all measurement for this grid were performed farther downstream relative to M. The far-field is hence identified as the region where there is no $\langle uv \rangle$, inhomogeneity of the mean flow, and production.

POWER-LAW DECAY OF ENERGY

The power-law decay of turbulent kinetic energy downstream of a grid, expressed in (1), may also be given by

$$\frac{\langle q^2 \rangle}{U^2} = A \left(\frac{U_0 t}{M} - \frac{U_0 t_0}{M} \right)^n \tag{4}$$

where A is a constant of proportionality, and $U_0 t_0 / M$ is the virtual origin. The power-law fitting technique introduced by Hearst & Lavoie (2014*a*) was employed here to determine the power-law fit unknowns. Power-law decay exponents of $n = -1.23$ and -1.32 were found for $Rd38$ and $Sq39$, respectively. In the far-field of $Fs39$ ($U_0 t / M \geq 17.0$), where the flow is approximately homogeneous, the estimated decay exponent is $n = -1.28$. Hence all far-field decay exponents are very similar and fall within -1.28 ± 0.05.

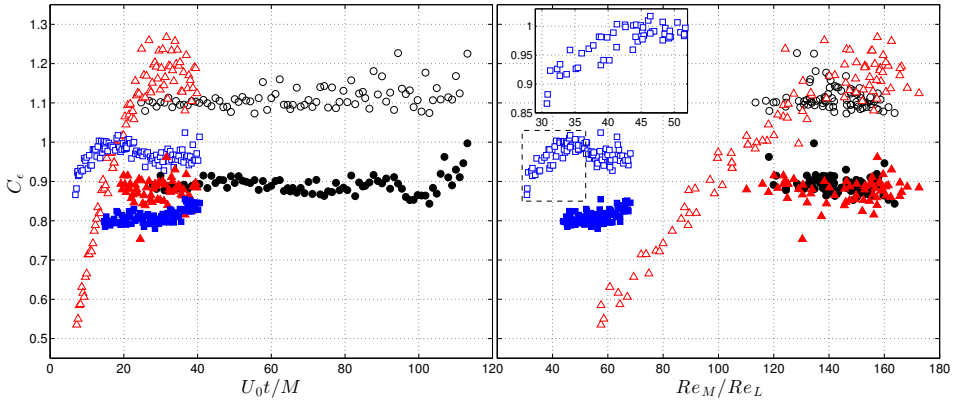

Figure 5. Normalized turbulent kinetic energy dissipation rate at $Re_M = 28{,}500$ estimated from isotropy using only $\langle u^2 \rangle$ (empty symbols) and more robustly from $\langle q^2 \rangle$ (filled symbols). Inset shows a region where C_ε from $Sq39$ approximately scales with Re_M/Re_L. (△) $Fs39$, (□) $Sq39$, (○) $Rd38$.

In the near-field of $Fs39$ ($U_0 t/M < 17.0$), where the flow is inhomogeneous and characterized by production and transverse transport, a decay rate of $n = -3.27$ was measured. This represents very rapid decay, however, this result is only for the specific axis measured. In the inhomogeneous region, one power-law is unlikely to describe the entire field's decay. Figure 4 illustrates the two phase decay in the wake of $Fs39$, where there is a clear distinction between the non-equilibrium near-field and the far-field.

NORMALIZED DISSIPATION RATE

The streamwise evolution of the normalized dissipation scaling, C_ε, is shown in Figure 5 for all three grids. The normalized dissipation is plotted against both streamwise position and Re_M/Re_L, the latter being the relationship proposed by Valente & Vassilicos (2012). All measurements in the wake of $Rd38$ are performed in the far-field, hence C_ε is approximately constant as per traditional expectations. Both of $Fs39$ and $Sq39$ approximately satisfy $C_\varepsilon \sim Re_M/Re_L$ before becoming approximately constant in the far-field.

Although there is no production at the first transverse measurement station for $Sq39$ ($x = 1.25$ m, $U_0 t/M = 17.0$), there is non-zero $\langle uv \rangle$ ahead of this position (Figure 3). If $\langle uv \rangle \neq 0$ is taken to mean the flow is not isotropic and is still evolving, then one might expect a non-equilibrium region, or at least a region of different development from the far-field, near $Sq39$, which indeed exists. Given that both $Sq39$ and $Fs39$ experience $\langle uv \rangle \neq 0$ near the grid, and this appears to correlate to the evolution of C_ε, we explicitly plot this correlation in Figure 6. In said figure, not only do we see that when $\langle uv \rangle$ becomes approximately constant, C_ε also becomes approximately constant, but that the results for all three grids lie on approximately the same line. While these results are for this specific setup and measurement axis, it nonetheless identifies that there is correlation between the evolution of $\langle uv \rangle$ and C_ε. However, identifying if this is a causal relationship is difficult. As such, in the next section, we investigate what other flow properties might be influenced by $\langle uv \rangle$.

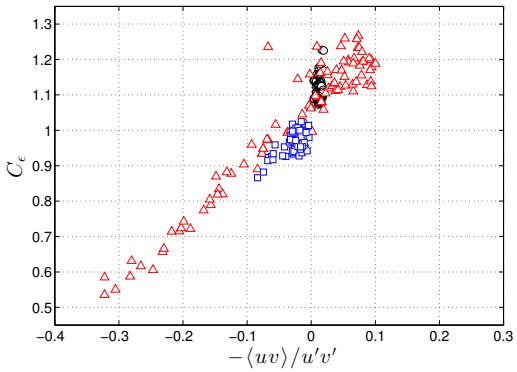

Figure 6. Relationship between normalized kinetic energy dissipation rate and the normalized Reynolds stress at $Re_M = 28{,}500$. (△) $Fs39$, (□) $Sq39$, (○) $Rd38$.

SPECTRA

The one-dimensional velocity spectra, $\langle u^2 \rangle = \int_0^\infty F_{11}\,\mathrm{d}k$, produced by the various grids at similar Re_λ are compared in order to ascertain if the spectral shape induced by the fractal geometry differs from that of the canonical grids. In Figure 7, spectra from the far-field of all three grids are compared at $Re_\lambda \approx 66$. For this Re_λ in the far-field the spectra produced by the three grids is not appreciably different, however, this Re_λ is fairly low. This limitation is due to the low Re_λ produced by $Rd38$, and as such from here forward we compare only $Sq39$ and $Fs39$.

Figure 8 compares non-equilibrium and far-field spectra at $Re_\lambda \approx 115$. Once again, the far-field spectra from both $Sq39$ and $Fs39$ are approximately collapsed, identifying that there is no significant difference in spectral shape for these two flows sufficiently far from the grid. However, two different non-equilibrium measurements near $Fs39$ produce a spectral shape with a scaling range closer to $k^{-5/3}$ than the far-field spectra at similar Re_λ. Thus Figure 8 identifies that the near $k^{-5/3}$ spectra observed in the wake of fractals is associated with the extended non-equilibrium region rather than the fractal nature of the grid itself, as sufficiently far from the grid the spectra generated by fractal and regular square mesh generators is practically the same.

To investigate the shape of spectra from the non-

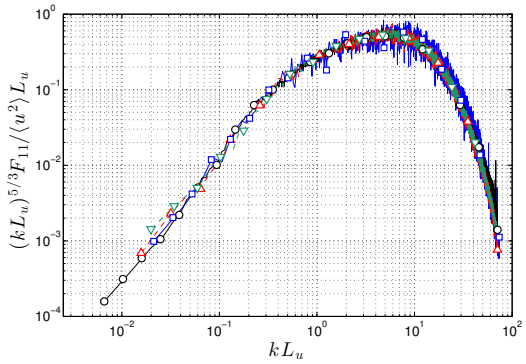

Figure 7. Compensated spectra at $Re_\lambda \approx 66$ in the far-field of each grid. (△) $Fs39$, $U_0t/M = 28.3$, $Re_M = 40{,}000$, $Re_\lambda = 65$; (▽) $Fs39$, $U_0t/M = 17.4$, $Re_M = 28{,}500$, $Re_\lambda = 66$; (□) $Sq39$, $U_0t/M = 32.2$, $Re_M = 17{,}500$, $Re_\lambda = 66$; (○) $Rd38$, $U_0t/M = 26.4$, $Re_M = 35{,}000$, $Re_\lambda = 66$.

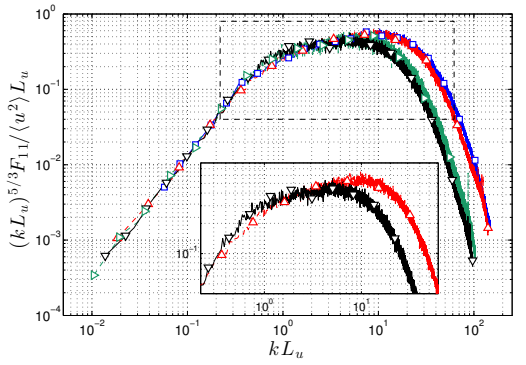

Figure 8. Compensated spectra at $Re_\lambda \approx 115$ in the non-equilibrium region and far-field. (□) $Sq39$, $U_0t/M = 19.5$, $Re_M = 44{,}000$, $Re_\lambda = 112$, far-field; (△) $Fs39$, $U_0t/M = 21.6$, $Re_M = 93{,}000$, $Re_\lambda = 113$, far-field; (▽) $Fs39$, $U_0t/M = 8.6$, $Re_M = 30{,}500$, $Re_\lambda = 116$, non-equilibrium; (▷) $Fs39$, $U_0t/M = 10.4$, $Re_M = 39{,}500$, $Re_\lambda = 117$, non-equilibrium. Only two cases are shown in the inset for clarity.

equilibrium region further, we plot the spectra from three different transverse positions in the non-equilibrium region of $Fs39$ at $Re_M = 88{,}500$ in Figure 9. These three positions were chosen to represent positions with local maxima, minima, and zero $\langle uv\rangle$. The figure illustrates that even for measurements within the non-equilibrium region, different scaling range slopes are achievable if $\langle uv\rangle$ is varied. However, in Figure 9 the location with $\langle uv\rangle \approx 0$ also has a lower Re_λ. To clarify that the scaling range slope is affected by $\langle uv\rangle$, we compare far-field and non-equilibrium spectra at $Re_\lambda = 180$ in Figure 10(a), where it is evident that for the same Re_λ we can achieve two very different spectral shapes depending on the level of $\langle uv\rangle$.

To further detail the correlation between $\langle uv\rangle$ and the shape of the spectrum, we plot the coherence spectrum, $\zeta_{12} = |F_{12}|^2/(F_{11}F_{22})$ in Figure 10(b). The coherence spectrum is a measure of the correlation between u and v for a given wavenumber. In Figure 10, the approximate scaling range is marked by dashed lines, and it is evident that there is non-zero coherence for wavenumbers that overlap with

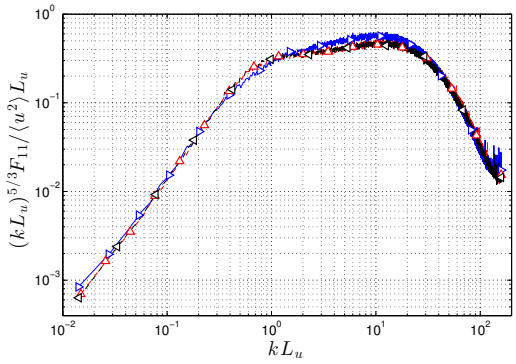

Figure 9. Compensated spectra at $U_0t/M = 10.9$ behind $Fs39$ with $Re_M = 88{,}500$. (▷) $y/M = 1.25$, $Re_\lambda = 134$, $\langle uv\rangle/U_0^2 \approx 0$; (△) $y/M = 1.00$, $Re_\lambda = 180$, $\langle uv\rangle/U_0^2 \approx 6\times 10^{-4}$; (◁) $y/M = -0.25$, $Re_\lambda = 180$, $\langle uv\rangle/U_0^2 \approx -6\times 10^{-4}$.

the scaling range for the non-equilibrium case. This identifies that $\langle uv\rangle$ penetrates to scales associated with the scaling range, which alters the spectral shape there and indicates that we do not have a sufficient separation of scales such that the large and small scales are independent. Thus, the Kolmogorov-based prediction of $k^{-5/3}$ is not applicable to this flow, and the appearance of a near $k^{-5/3}$ scaling range is either coincidental or requires an alternative derivation.

Returning to Figure 9 it is also worth considering how the non-equilibrium spectrum with $\langle uv\rangle \approx 0$ compares to a far-field spectrum at the same Re_λ, also with $\langle uv\rangle \approx 0$. This is illustrated in Figure 11(a), where we see that the non-equilibrium spectrum from $Fs39$ and far-field spectrum from $Sq39$, both at $Re_\lambda = 134$, are approximately collapsed if $\langle uv\rangle \approx 0$. Figure 11(b) verifies that indeed there is no coherence at scales that overlap with the scaling range. This strongly suggests that it is indeed spectral forcing from $\langle uv\rangle$ that moves the spectrum closer to $k^{-5/3}$ in the present flow.

CONCLUSIONS

The major findings of this work can be summarized as follows:

(i) In the far-field, the power-law decay exponent is not appreciably different for the three grids tested here, i.e., $n = -1.28 \pm 0.05$.

(ii) While C_ε grows in the non-equilibrium region, where it is approximately described by $C_\varepsilon \sim Re_M/Re_L$, it becomes approximately constant sufficiently far from all three grids.

(iii) The evolution of C_ε is strongly correlated to $\langle uv\rangle/u'v'$ in the present flow.

(iv) In the far-field of all three grids, the produced one-dimensional spectra are not appreciably different for the three grids for a given Re_λ.

(v) The difference between a non-equilibrium and a far-field spectrum appears to be related to $\langle uv\rangle$ that penetrates to scales associated with the scaling range. If $\langle uv\rangle \approx 0$, then non-equilibrium and far-field spectra are not significantly different from one another.

These findings suggest that the nature of multi-scale fractal and regular grid turbulence may not be fundamentally different, given that the far-field results are remarkably similar across all three grids. The changes in C_ε and the spectra in

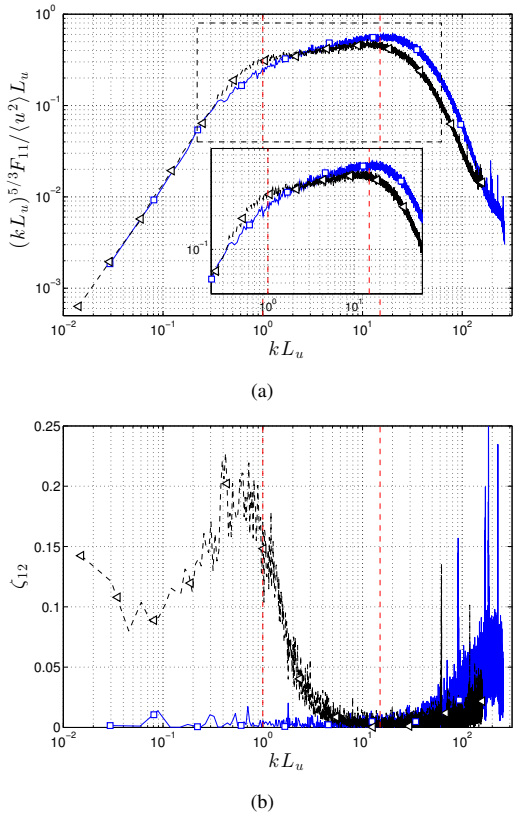

Figure 10. Comparison of (a) compensated spectra and (b) spectral coherence as measured in the non-equilibrium region and the far-field at $Re_\lambda = 180$ and with contrasting levels of $\langle uv\rangle$. ($\triangleleft$) $Fs39$, $U_0t/M = 10.9$, $y/M = -0.25$, $Re_M = 88,500$, non-equilibrium; ($\square$) $Sq39$, $U_0t/M = 17.0$, $y/M = 0.15$, $Re_M = 84,500$, far-field. Vertical lines roughly highlight the scaling range. F_{11} is measured using a single-wire and ζ_{12} is measured with a X-wire.

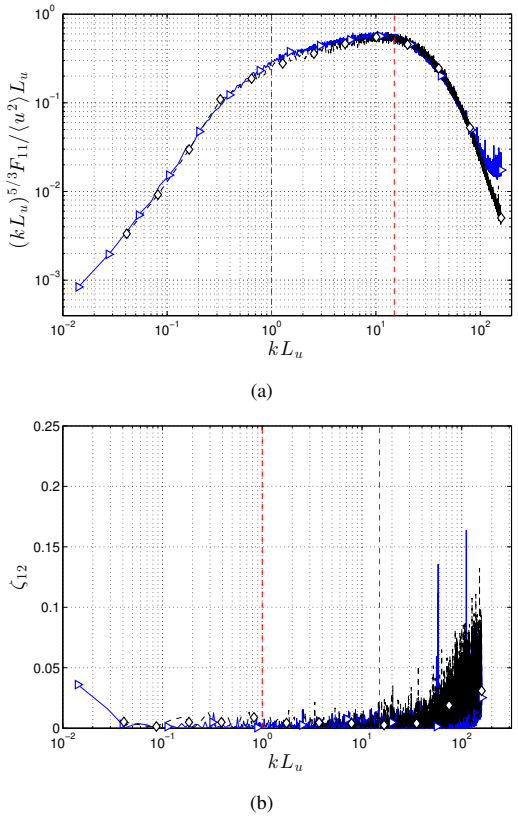

Figure 11. Comparison of (a) compensated spectra and (b) spectral coherence as measured in the non-equilibrium region and the far-field at $Re_\lambda = 134$ and with $\langle uv\rangle \approx 0$. ($\triangleright$) $Fs39$, $U_0t/M = 10.9$, $y/M = 1.25$, $Re_M = 88,500$, non-equilibrium; ($\diamond$) $Sq39$, $U_0t/M = 27.8$, $y/M = 0.15$, $Re_M = 70,500$, far-field. Vertical lines roughly highlight the scaling range. F_{11} is measured using a single-wire and ζ_{12} is measured with a X-wire.

the non-equilibrium region appear to correlate to the local $\langle uv\rangle$, which is able to exert influence on scales that overlap with the scaling range. This suggests that the entire flow field can be captured in one physical model; this could be a more robust version of either the non-equilibrium or equilibrium model.

REFERENCES

Comte-Bellot, G. & Corrsin, S. 1966 The use of a contraction to improve the isotropy of grid-generated turbulence. *J. Fluid Mech.* **25** (4), 657–682.

Goto, S. & Vassilicos, J. C. 2015 Energy dissipation and flux laws for unsteady turbulence. *Phys. Lett. A* **379**, 1144–1148.

Hearst, R. J. & Lavoie, P. 2014*a* Decay of turbulence generated by a square-fractal-element grid. *J. Fluid Mech.* **741**, 567–584.

Hearst, R. J. & Lavoie, P. 2014*b* Scale-by-scale energy budget in fractal element grid-generated turbulence. *J. Turb.* **15** (8), 540–554.

Hurst, D. & Vassilicos, J. C. 2007 Scalings and decay of fractal-generated turbulence. *Phys. Fluids* **19** (035103).

Isaza, J. C., Salazar, R. & Warhaft, Z. 2014 On grid-generated turbulence in the near- and far field regions. *J. Fluid Mech.* **753**, 402–426.

Krogstad, P.-A. & Davidson, P. A. 2012 Near-field investigation of turbulence produced by multi-scale grids. *Phys. Fluids* **24** (035103).

Mazellier, N. & Vassilicos, J. C. 2010 Turbulence without Richardson-Kolmogorov cascade. *Phys. Fluids* **22** (075101).

Nagata, K., Sakai, Y., Inaba, T., Suzuki, H., Terashima, O. & Suzuki, H. 2013 Turbulence structure and turbulence kinetic energy transport in multiscale/fractal-generated turbulence. *Phys. Fluids* **25** (065102).

Valente, P. C. & Vassilicos, J. C. 2011 The decay of turbulence generated by a class of multiscale grids. *J. Fluid Mech.* **687**, 300–340.

Valente, P. C. & Vassilicos, J. C. 2012 Universal dissipation scaling for nonequilibrium turbulence. *Phys. Rev. Lett.* **108** (214503).

Valente, P. C. & Vassilicos, J. C. 2014 The non-equilibrium region of grid-generated decaying turbulence. *J. Fluid Mech.* **744**, 5–37.

Vallikivi, M., Hultmark, M., Bailey, S. C. C. & Smits, A. J. 2011 Turbulence measurements in pipe flow using a nano-scale thermal anemometry probe. *Exp. Fluids* **51**, 1521–1527.